



OPEN Spatial transcriptomics reveals tumor microenvironment heterogeneity in EBV positive diffuse large B cell lymphoma

Mei-yao He^{1,3}, Meng Liu^{2,3}, Jiayin Yuan^{1,3}, Jin Lv¹, Wei Li¹, Qianwen Yan¹, Yujiao Tang¹, Luyi Wang¹, Li Guo¹ & Fang Liu¹✉

Accumulating research suggests that Epstein-Barr Virus-positive Diffuse Large B-cell Lymphoma (EBV+DLBCL) is associated with immune dysfunction and tumor microenvironment (TME) heterogeneity. While the prognostic role of the TME in EBV-DLBCL is established, its impact on EBV+DLBCL survival remains unclear. Here, we integrated 10X Visium spatial transcriptomics (ST) with single-cell RNA sequencing (scRNA-seq) to map TME heterogeneity in EBV+DLBCL. Gene Ontology (GO) and Kyoto Encyclopedia of Genes and Genomes (KEGG) analyses identified PD-1/PD-L1 signaling as a hallmark of EBV+DLBCL's immunosuppressive TME. Functional validation using the PD-1/PD-L1 inhibitor BMS202 revealed dose-dependent suppression of proliferation and enhanced apoptosis in EBV+Farage cells, with TLR4 emerging as a downstream effector showing EBV-status-dependent regulation. These findings not only link TME-driven PD-1/PD-L1 activation to EBV+DLBCL's poor prognosis but also provide preclinical evidence for PD-1/PD-L1 blockade as a therapeutic strategy.

Keywords DLBCL, EBV infection, TME, PD-1/PD-L1, Spatial transcriptomics

EBV+DLBCL stands as a notable and distinct subtype within the spectrum of DLBCL, primarily distinguished by its intimate association with EBV infection^{1,2}. This intriguing subset has garnered substantial attention due to its distinctive biological attributes and clinical behaviours that set it apart from EBV-DLBCL. EBV+DLBCL, characterized by the presence of EBV within tumor cells, introduces a complexity that influences both disease pathogenesis and treatment responses. Its intricate interplay with the host immune system further accentuates its uniqueness. An inherent challenge in the management of EBV+DLBCL lies in its propensity for limited responses to traditional chemotherapy regimens, thereby contributing to a less favourable prognosis compared to EBV-DLBCL^{2,3}. The recurrent scenario of diminished treatment efficacy and compromised recovery underscores a critical need for innovative and tailored therapeutic strategies.

In our earlier study of DLBCL, substantial intra-tumor heterogeneity was observed at both the genetic and phenotypic levels⁴. Genetically, diverse mutations, amplifications, and translocations may occur among distinct tumor cell populations. This genetic diversity can lead to distinct pathways of disease progression, response to therapy, and potential drug resistance⁵. Phenotypically, EBV+DLBCL tumors can consist of various subclones with differing protein expression patterns, making targeted therapeutic approaches challenging. This intrinsic heterogeneity presents obstacles for treatment efficacy. Conventional treatment methods, like chemotherapy, may effectively target certain tumor cell populations while leaving others unaffected, fostering relapse and disease recurrence. Precision medicine approaches that focus on specific molecular vulnerabilities might miss certain subclones, diminishing their effectiveness^{6,7}. The TME contributes further to EBV+DLBCL heterogeneity. The emergence of EBV within DLBCL introduces a multifaceted interplay between viral elements, immune effectors, and tumor cells, while the interactions between malignant cells, immune cells, stromal cells, and signaling molecules within the TME can be highly variable. This shows the TME of EBV+DLBCL demonstrates unique features⁸. Understanding the interplay between tumors and the immune system has laid the groundwork for informed patient stratification, guiding surgical strategies logically. Additionally, it has deepened our grasp of potential intervention junctures and the factors contributing to treatment ineffectiveness.

¹Department of Pathology, The First People's Hospital of Foshan, Foshan 528000, People's Republic of China.

²School of Life and Health Technology, Dongguan University of Technology, Dongguan 523808, People's Republic of China. ³Mei-yao He, Meng Liu and Jiayin Yuan have equally contributed to this work. ✉email: gyluifang@hotmail.com

While the substantial heterogeneity within the TME continues to pose a significant obstacle in comprehending and treating cancers. This underscores the importance of comprehensively delineating the composition and functional dynamics of the tumor-immune interaction within the TME. Numerous endeavors have illuminated certain disparities in TME heterogeneity and concurrent alterations associated with malignancies across diverse cancer categories. Nevertheless, the bulk of research has primarily centered on TME composition and gene expression, often overlooking the critical aspect of its spatial distribution specificity⁹. Therefore, clarifying the distribution characteristics of TME of EBV+DLBCL combined with new technology is helpful to explore the key pathogenesis and innovative therapeutic approaches.

ST, as highlighted in recent literature, offers a nuanced exploration of tissue heterogeneity and cellular dynamics. By preserving the spatial context of gene expression, this methodology allows for the identification of distinct cell populations and their functional roles within specific tissue microenvironments^{10,11}. For instance, a study by Vickovic et al. employed spatial transcriptomics to unveil spatially restricted gene expression patterns in the mouse brain, shedding light on the regional specialization of neuronal subtypes¹². Furthermore, the advantages extend to dissecting intricate cellular interactions. A notable example is the work by Eng et al., which employed spatial transcriptomics to elucidate the spatial organization of immune cells in the TME¹³. This approach revealed spatially distinct gene expression profiles associated with immune cell subsets, contributing to a deeper understanding of the immune response in cancer. ST, as evidenced by these studies, emerges as a powerful tool for unraveling the spatial intricacies of gene expression, providing valuable insights into tissue-specific functions and cellular interactions.

In this study, we pioneer the integration of published DLBCL scRNA-seq data⁹ with ST to systematically map TME heterogeneity in EBV+ and EBV-DLBCL. By aligning scRNA-seq-defined cellular subtypes with their spatial distributions in ST datasets, we identified EBV-specific TME architectures and functionally validated the PD-1/PD-L1 axis as a hallmark of immunosuppression in EBV+DLBCL. Our mechanistic investigations revealed that PD-1/PD-L1 blockade using BMS202 exerts dose-dependent anti-tumor effects and induces EBV-status-dependent TLR4 modulation. These findings not only establish TME-driven PD-1/PD-L1 activation as a key determinant of EBV+DLBCL progression but also provide a spatial-omics framework for developing precision immunotherapies targeting this axis.

Materials and methods

Patients' sources

236 cases of DLBCL were collected from The First People's Hospital of Foshan between July 2017 and July 2020. All cases underwent in situ hybridization for EBV-encoded mRNA (EBER) and met the World Health Organization diagnostic criteria. The patient with other immunodeficiency causes and the diagnosis of EBV+ diffuse large B-cell lymphoma, EBV+ Hodgkin's lymphoma, EBV+ pleomorphic lymphoproliferative disorders, or any previous lymphoma-related treatment were excluded. In all cases, the diagnosis was established independently by three hematopathologists⁴, and a consensus diagnosis was reached according to the criteria defined by the 2016 World Health Organization classification of lymphoid neoplasms. Clinical information of EBV+ ($N=23$) and EBV- patients ($N=30$), including sex, age, LDH level, B symptoms, Ann Arbor stage, anatomic locations, IPI score, and survival time, were collected for comparison. Complete clinical information and follow-up data were gathered, with all patients being followed up from the date of diagnosis until July 2020. All patients received R-CHOP-based chemotherapy and a basic supportive regimen.

To ensure the sequencing quality and avoid DNA degradation, we selected only formalin-fixed paraffin-embedded (FFPE) samples from the last 2 years for further ST analysis using Visium 10x technology. Among these cases, we chose 4 cases of EBV+ and 4 cases of EBV- respectively, which had complete specimens comprising more than 50% tumor cells and < 10% necrosis tissues, for ST analysis.

In situ hybridization for EBV

In situ hybridization for EBERs was performed on deparaffinized 4 μ m-thick FFPE tissue sections using EBER Detection Kit (ISH-7001, Suzhou, China) following the manufacturer's protocol. All slides were examined using a standard bright-field microscope by two independent pathologists. Positive staining was identified by a yellow to brown colour in the nucleus. In this study, cases with > 80% EBER-positive malignant cells were classified as EBV+DLBCL¹⁴.

Immunohistochemistry (IHC)

The tissues were subjected to deparaffinization using xylene, followed by rehydration. Antigen retrieval was performed by heating the sections in citrate buffer (pH 6.0). Subsequently, the sections were incubated with PD-L1 antibody (1:200; Abcam; ab205921; New Territories, HK) overnight on a shaker at 4 °C. After extensive washing, the sections were exposed to horseradish peroxidase (HRP) goat anti-rabbit IgG secondary antibody (1:400, EarthOx, 7074 S, Millbrae, USA) for 2.5 h at room temperature in a dark box and then conjugated to DAB (Maixin, Fuzhou, China). Following immunostaining, the sections were counterstained with haematoxylin.

Cell lines and culture

The EBV+DLBCL cell line Farage (CRL-2630)¹⁵ and EBV-DLBCL cell line DB (CRL-2289) were obtained from the American Type Culture Collection (ATCC, Manassas, VA, USA). Both cell lines were maintained in RPMI-1640 medium (Gibco, Shanghai, China) supplemented with 10% fetal bovine serum (FBS), and incubated at 37 °C and 5% CO₂. For experimental treatments, cells were exposed to BMS202 (PD-1/PD-L1 signaling inhibitors) at concentrations of 5 μ M, 10 μ M, and 20 μ M for 24 h.

Cholecystokinin-8 (CCK8) assays

DB and Farage cells (control, 5 μ M BMS202, 10 μ M BMS202 and 10 μ M BMS202 group) were seeded into 96-well plates. These cells (1×10^6 cells/mL) were maintained in RPMI-1640 + 10% fetal bovine serum at 37 °C and 5% CO₂. The cell viability was assessed using CCK8 assay. Briefly, 10 μ L of CCK8 reagent (Dojindo, Kumamoto, Japan) was added to the 96-well plates and incubated continually for 12 h at 37 °C. The absorbance values were measured at 450 nm using a Bio-Rad model 450 microplate reader (Bio-Rad, Hercules, CA, USA). The cell viability was indirectly determined by examining the ratio of the absorbance value of BMS202 treated cells relative to the control cells, from these experiments.

Quantitation of apoptotic cells

Annexin V-FITC (BD Bioscience, USA) and PI double staining were used to identify and quantify apoptotic cells present in the DB and Farage cells (control and 10 μ M BMS treated for 24 h). Briefly, the cells were collected and resuspended in cold PBS at a density of 1×10^6 cells/mL and then introduced into 200 μ L of the Annexin V-binding buffer. The samples were then incubated with 2 μ L fluorescein isothiocyanate (FITC)-labeled Annexin V and 2 μ L PI at room temperature for 15 min and immediately analyzed by a FACS Calibur flow cytometer (BD, NJ, USA). The acquired data were evaluated using FCS-Express software version 3.0 (De Novo).

Apoptotic cells in DB and Farage cell lines, including untreated controls and 10 μ M BMS202-treated groups (24 h exposure), were quantified using Annexin V-FITC/PI dual staining (Annexin V-FITC Apoptosis Detection Kit I, BD Biosciences, San Jose, CA, USA). Briefly, cells were harvested, washed twice with ice-cold PBS, and resuspended in $1 \times$ Binding Buffer at 1×10^6 cells/mL. Aliquots of 200 μ L cell suspension were incubated with 2 μ L FITC-conjugated Annexin V and 2 μ L propidium iodide (PI) in the dark (25 °C, 15 min). Flow cytometric analysis was immediately performed using a BD FACS Calibur™ system (BD Biosciences), with 10,000 events acquired per sample. Data analysis was conducted using FCS Express 7 Flow Cytometry Software (De Novo Software, Glendale, CA, USA), with apoptotic populations defined as Annexin V⁺/PI⁻ (early apoptosis) and Annexin V⁺/PI⁺ (late apoptosis).

RNA isolation and quantitative PCR (qPCR)

Total RNA was isolated from control and BMS202-treated DB or Farage cells using TRIzol[®] Reagent (Thermo Fisher Scientific, Waltham, MA, USA), followed by DNase I treatment (TaKaRa Bio, Shiga, Japan) to eliminate genomic DNA. RNA quality was verified by NanoDrop 2000 spectrophotometry ($A_{260}/A_{280} > 1.8$).

For qRT-PCR validation, first-strand cDNA was synthesized from 1 μ g total RNA using the SuperScript[™] III Reverse Transcriptase kit (Thermo Fisher Scientific) in 20 μ L reactions (42 °C for 50 min; 70 °C for 15 min). Target genes were amplified using gene-specific primers (Table.S3) in 25 μ L PCR mixtures containing 2 \times Taq Master Mix (Vazyme, Nanjing, China). Amplification was performed on a Bio-Rad S1000™ Thermal Cycler (Hercules, CA, USA) under standardized conditions: initial denaturation at 95 °C for 3 min; 35 cycles of 95 °C/30 s, [Primer-specific TM] °C/30 s, 72 °C/45 s; final extension at 72 °C for 5 min¹⁶.

ST experiments

FFPE tumor samples were prepared following the recommended protocols for tissue preparation (tissue preparation guide CG000408). H&E image preparation was carried out following the protocol (including Deparaffinization, H&E staining, Imaging, and decrosslinking, CG000408). Libraries were then prepared based on the Visium Spatial Gene Expression User Guide. The libraries were loaded at 300 pM and subjected to sequencing on a NovaSeq 6000 System (Illumina) using a NovaSeq S4 Reagent Kit (200 cycles, 20027466, Illumina) to achieve a sequencing depth of approximately 320 M read pairs per sample. The sequencing process followed this read protocol: read 1, 28 cycles; i7 index read, 10 cycles; i5 index read, 10 cycles; read 2, 91 cycles¹⁷.

Spatial transcriptomics data processing

FASTQ files and manually aligned histology images were processed using Space Ranger 1.3.0 (10x Genomics) with the Visium Human Transcriptome Probe Set v1.0 (GRCh38-2020-A). Raw gene-spot matrices were filtered to retain spots with > 2,000 genes and > 10,000 UMIs, yielding 34,795 high-quality spots for downstream analysis. All data were deposited in the National Omics Data Encyclopedia (NODE; Project ID OEP004742). To address potential batch effects, we implemented an integration approach using the Harmony algorithm¹⁸. The datasets were initially combined into a unified Seurat object through the merge function, followed by normalization with SCTransform. During normalization, we selected the 3,000 most variable features based on residual variance for downstream analysis. Principal component analysis was conducted on the normalized expression matrix prior to Harmony integration. For batch correction, we applied the RunHarmony function with standard parameters, specifying the SCT assay for input data and designating sample IDs as the grouping variable. The integrated dataset was subsequently analyzed using Seurat's standard workflow, where we employed the first 40 Harmony-corrected dimensions for both UMAP visualization and Leiden clustering (resolution = 0.35). Cluster identities were determined through manual annotation guided by differentially expressed markers, which were identified using a Wilcoxon rank-sum test with thresholds of 25% minimum expression fraction and a log₂ fold-change cutoff of 0.25 (Fig. 1).

For gene set enrichment analysis (GSEA), the GO and KEGG pathway datasets^{19,20} were used. Protein-protein interaction (PPI) network analysis was performed using STRING (Search Tool for the Retrieval of Interacting Genes/Proteins; <https://string-db.org>).

Spatial cell typing with cell2location

We used cell2location²¹ to deconvolute the cellular composition of each capture area (spot), a Bayesian framework that leverages annotated single-cell RNA sequencing (scRNA-seq) reference data to probabilistically estimate

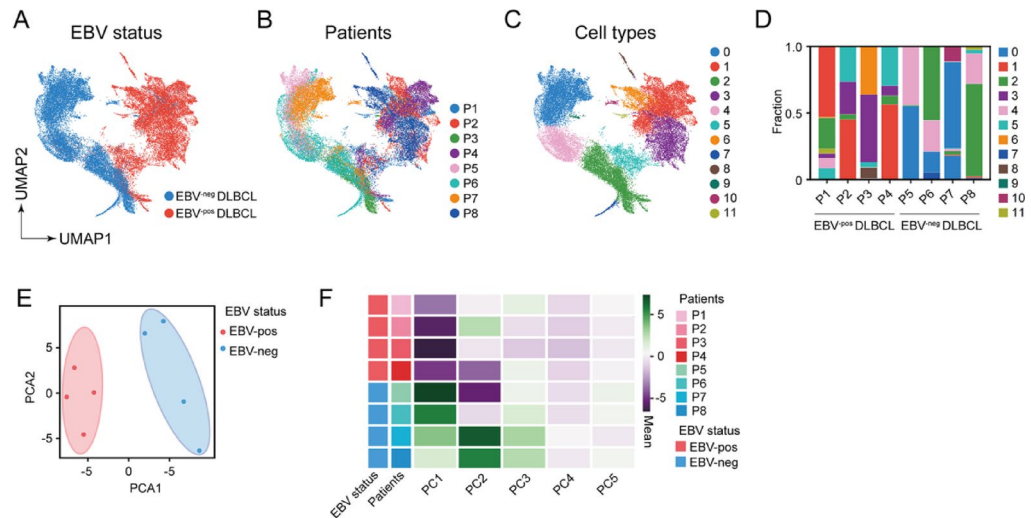


Fig. 1. Different patterns of EBV+DLBCL and EBV-DLBCL spatial heterogeneities. (A–B) UMAP (Uniform Manifold Approximation and Projection) plot of spots from all samples, colored by their EBV status (A) and patients (B). (C) UMAP of the spots colored by cluster identities. (D) Fraction of clusters in each sample. (E–F) PCA of EBV+ and EBV-DLBCL (E), Spatial distribution similarity comparison of the patients across different EBV statuses (F).

cell-type proportions within each spatial transcriptomics spot. For this analysis, we integrated our 10X Visium spatial transcriptomics profiles with a published DLBCL scRNA-seq atlas⁹ as the reference dataset, enabling spatially resolved cell-type mapping throughout the tissue microenvironment.

Ligand–receptor colocalization analysis

Our analysis of Ligand-Receptor Analysis was performed using the stLearn package²². First, we established expression thresholds for each gene in the LR pairs across quality-controlled Visium spots. Gene expression was considered positive when the cell2location-derived abundance estimates exceeded the median expression level for that gene within the tissue section. For each patient sample, we systematically quantified co-expression patterns of LR pairs by comparing tumor regions with adjacent background tissue. This generated binary matrices that were statistically evaluated using χ^2 tests of independence. To account for multiple hypothesis testing across all analyzed LR pairs, we implemented Bonferroni correction with a stringent significance threshold (adjusted $p < 0.05$). Only LR pairs demonstrating consistent tumor-specific enrichment patterns (observed in ≥ 2 independent patient samples) were considered biologically significant.

Data analysis

Statistical analyses for all the experimental data generated were performed using the SPSS 26.0 statistical package. The data are presented as the mean \pm SD. The construction of statistical charts was performed using the GraphPad Prism 8 software package (GraphPad Software, CA, USA). All data were analysed using the Mann-Whitney U test, t-test and, when performing more than five simultaneous statistical comparisons or Exploratory analysis scenarios, the application of Bonferroni adjustment for multiple hypothesis testing. For pre-specified confirmatory hypothesis testing, we reported raw p-values with the prespecified significance threshold ($p < 0.05$). $p < 0.05$ was considered statistically significant.

Ethics approval and consent to participate

All experimental protocols were approved by Ethics Committee of the First People's Hospital of Foshan, approval no. 2023-NO. 143), and with the 1964 Helsinki Declaration and its later amendments. Informed consent was obtained from all individual participants included in the study. This article does not contain any animal studies.

Results

Clinical characteristics show that EBV-infected DLBCL patients have a poor prognosis

From the records of our institutions, between July 2017 and July 2020, more than 80% of neoplastic cells in 23 out of 236 (9.7%) cases of diffuse large B-cell lymphomas (DLBCL) showed EBV infection, as detected by EBER in situ hybridization (Fig. S1). Among the 23 EBV+DLBCL patients, the male-to-female ratio was 1.1:1, and 14 (60.87%) patients were aged over 60 years. 13 patients (56.52%) exhibited an increased level of lactate dehydrogenase (LDH). Only 6 patients (26.09%) presented with B symptoms. 6 patients (69.57%) were classified as having an advanced stage based on the Ann Arbor stage. Regarding the anatomical sites of tumors, 14 patients (60.87%) had extra nodal involvement, including the spleen (21.74%), soft tissue (4.35%), gastric region (8.70%), colon (4.35%), tonsil (13.04%), and nasal cavity (8.70%). The International Prognostic Index (IPI) score revealed that 5 patients (21.74%) were classified as low risk (0–1 point), 11 (47.83%) as medium risk (2–3 points), and 7 (30.43%) as high risk (4–5 points). Following R-CHOP-based chemotherapy, the median survival time was

17 months, ranging from 2 to 33 months. Patients with EBV+DLBCL demonstrated a shorter overall survival ($P<0.05$) compared to 30 randomly selected cases of DLBCL (Table.S1). The difference in prognosis urged us to explore Spatial heterogeneity in DLBCL caused by EBV infection.

Spatial heterogeneity between EBV+ and EBV-DLBCL

To comprehensively compare the spatial heterogeneity between EBV+ and EBV-DLBCL, we collected 8 tissue specimens from eight patients including four cases of EBV+DLBCL and four cases of EBV-DLBCL from a total of 236 patients for ST analysis using Visium 10x technology. The clinical information of these cases was stored in Table 1. In this study, the ST technology utilized spots with a diameter of 55 μm , containing approximately 8 to 20 cells. Each section encompassed up to 5000 spots within the capture area of 6.5 mm by 6.5 mm. The data revealed that the median sequencing depth of a single spot was approximately 5000 ~ 10,000 unique molecular identifiers (UMIs) and 1000 ~ 3000 genes (Fig. S2).

Integrated clustering analysis of ST data from all samples using Scanpy revealed 12 distinct clusters. Notably, the spot types between EBV+DLBCL and EBV-DLBCL showed significant differences (Fig. 1A-D). Additionally, we conducted a comparison of “pseudo bulk” data between EBV+DLBCL and EBV-DLBCL reference data within the same cancer type, and the results demonstrated a high level of compatibility (Fig. 1E-F). This suggests that EBV infection has a significant effect on the spatial cell type composition and distribution in DLBCL.

TME heterogeneity between EBV+ and EBV-DLBCL

Considering the tumor heterogeneity and individual differences among patients, we conducted individual section analysis to ensure the accuracy of our results. Cell type of published DLBCL scRNA-seq⁹ was used to score each spot for spatial omics sequencing data after inspection and clustering, and the cell type with the highest score for each cluster was used for annotation (Fig. S3). Through the gene expression and the score of tumor cells, T cells and monocytes¯ophages (Mo-Macro) (Fig. S4), we confirmed that the accuracy of cell annotation by Cell2 location.

To gain a deeper understanding of the distribution of cell types and their spatial organisation, we mapped the identified clusters back to their respective spatial locations, revealing distinct patterns that correlated with anatomical annotations (Fig. 2A). To delve deeper into the specific functions of each tumor cluster, we performed a differential gene expression (DEG) analysis for each cell cluster using annotated ST data. Subsequently, we conducted GO enrichment analysis for all DEGs within each cancer cell cluster, and we identified the top 10 GO terms that best represent the functions of each cluster of cancer cells. We meticulously researched the upper-level pathways of each term individually using the GO official website. Subsequently, we employed the highest parent pathway to consolidate the pathways and categorized each cluster of cancer cells based on their similar functions, specifically referring to their roles in the tumor (Fig. 2B, Table. S2).

To assess whether the tumor was in a passive defensive or aggressive state relative to the immune cells in the microenvironment, we performed GSVA for immune regulation pathways in tumor of each sample. The findings revealed that both positive and negative immune responses in EBV+DLBCL were stronger compared to EBV-DLBCL. Moreover, it is very interesting that, except patient 4 (P4), negative immune responses were stronger than positive immune responses in other 3 cases in EBV+DLBCL (Fig. 2C). This observation also suggests that a larger proportion of patients with EBV+ experienced a loss of immune cell surveillance and were in a state of negative immune regulation.

PD-1/PD-L1 is a significant ligand-receptor in the TME of EBV+DLBCL

We analyzed differential expression genes (DEGs) in the tumor regions of the EBV+ and EBV-DLBCL. To filter the DEGs, we set a Log2 fold-change ($|\log_2\text{FC}|$) of >1 and an adjusted p-value of <0.05 as the criteria. We found significant differences in the PD-1/PD-L1 immune response-related signaling pathway amongst the up-regulated genes (Fig. 3A-B). To verify this speculation, PD-L1 IHC staining was implemented on transverse sections of EBV+ and EBV-DLBCL. The results indicated that PD-L1 expression in EBV+DLBCL was significantly increased compared with EBV-DLBCL (Fig. 3C-D). To observe the spatial expression pattern of PD-1/PD-L1 in the tumor region, we mapped the expression of PD-1 and PD-L1 genes onto tissue slices. The results showed that both PD-1 and PD-L1 were highly expressed in EBV+DLBCL tumor areas, while they were dispersed in EBV-DLBCL (Fig. 3E-F). This suggests that the PD-1/PD-L1 signaling pathway has significant spatial heterogeneity in EBV+DLBCL and EBV-DLBCL. We utilized stLearn to perform Ligand-Receptor analysis (Fig. 3G), which

Sample	Age	Sex	Groups	LDH	B symptoms	Ann Arbor stage	Location	IPI score
P1	63	Female	EBV-pos DLBCL	Elevated	Absent	IIIA	Nodal	3
P2	68	Male	EBV-pos DLBCL	Elevated	Absent	IVA	Extra nodal	5
P3	60	Female	EBV-pos DLBCL	Normal	Absent	IVA	Nodal	3
P4	11	Male	EBV-pos DLBCL	Elevated	Present	IIIB	Extra nodal	3
P5	36	Male	EBV-neg DLBCL	Elevated	Absent	IIIA	Extra nodal	3
P6	64	Male	EBV-neg DLBCL	Elevated	Absent	IIIA	Nodal	3
P7	68	Female	EBV-neg DLBCL	Elevated	Absent	IVA	Nodal	4
P8	67	Female	EBV-neg DLBCL	Elevated	Absent	IIA	Nodal	2

Table 1. Clinicopathological features of 8 patients with EBV+ or EBV-DLBCL by Spatial transcriptome.

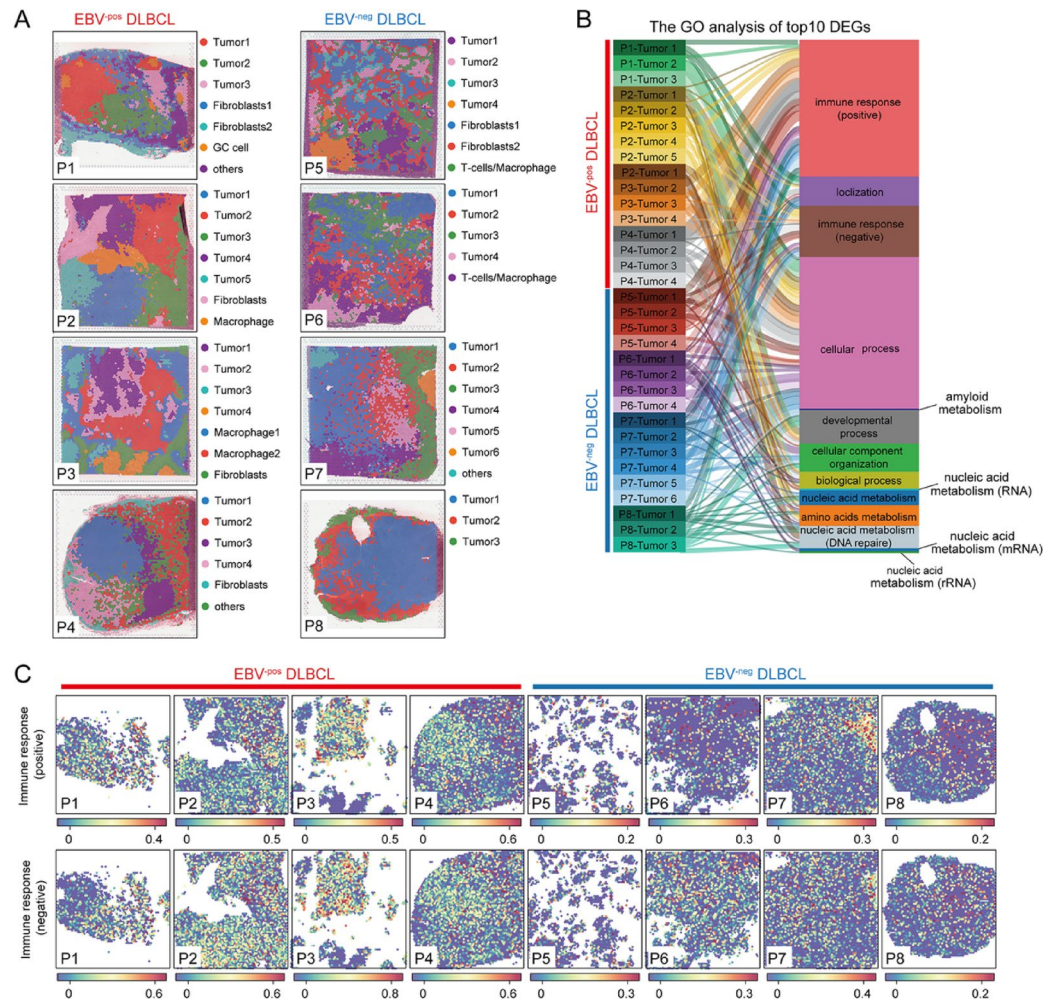


Fig. 2. Different patterns of EBV+DLBCL and EBV-DLBCL spatial heterogeneities. **(A)** The cell subsets of EBV+ and EBV-DLBCL and their spatial distribution. **(B)** The analysis of GO pathways for the top 10 DEGs in each tumor cell subpopulation of both EBV+ and EBV-DLBCL. **(C)** Evaluation of the immune regulation status of each tumor cell from EBV+ and EBV-DLBCL.

provided further confirmation that PD-1/PD-L1 is a significant Ligand-Receptor. Immune cells from different tumor areas were analyzed to determine which immune cells PD-1/PD-L1 is primarily regulated by. Our findings showed that in EBV+DLBCL, the primary immune cells involved are Mo-Macro, while in EBV-DLBCL, the main ones are follicular helper T (TFH) cells (Fig. 3H). It can be seen that in DLBCL, the differences in PD-1/PD-L1 signals caused by different states of EBV come from different immune cell regulation.

PD-1/PD-L1 signaling promote tumor cell proliferation and/or inhibit apoptosis in EBV+DLBCL

BMS202 treatment induced dose-dependent inhibition of cell proliferation and viability in both cell lines, with more pronounced effects observed in Farage cells (Fig. 4A). The CCK8 analysis revealed that Farage cells exhibited significant reduction in proliferation and viability at all tested concentrations (5 μ M: $p < 0.05$; 10–20 μ M: $p < 0.001$) (Fig. 4C), whereas DB cells showed only a non-significant downward trend at 5 μ M and achieved statistical significance at higher concentrations (10 μ M: $p < 0.05$; 20 μ M: $p < 0.01$) (Fig. 4B). The observed growth inhibition correlated with effective blockade of PD-1/PD-L1 signaling (Fig. 4D). These differential responses suggest that the greater dependence of Farage cells on PD-1/PD-L1 signaling comes from the overexpression of PD-1/PD-L1 signaling in Farage cells themselves. Flow cytometry analysis confirmed that 10 μ M BMS202 significantly induced apoptosis in both cell types (DB cells, $p < 0.05$; Farage cells, $p < 0.01$) (Fig. 4E–F), with Farage cells demonstrating particularly robust apoptotic response following PD-1/PD-L1 pathway inhibition, further supporting the pathway's critical role in Farage cells.

To investigate the potential link between PD-1/PD-L1 signaling and EBV+DLBCL, bioinformatics analysis was employed to depict the protein–protein interaction network, from which TLR4 was identified (Fig. 4G). Quantitative PCR analysis revealed distinct TLR4 expression patterns following PD-1/PD-L1 blockade. Farage cells demonstrated constitutively high TLR4 expression, which was significantly downregulated upon BMS202 treatment ($p < 0.001$). In contrast, DB cells showed opposite regulation, with TLR4 expression being markedly

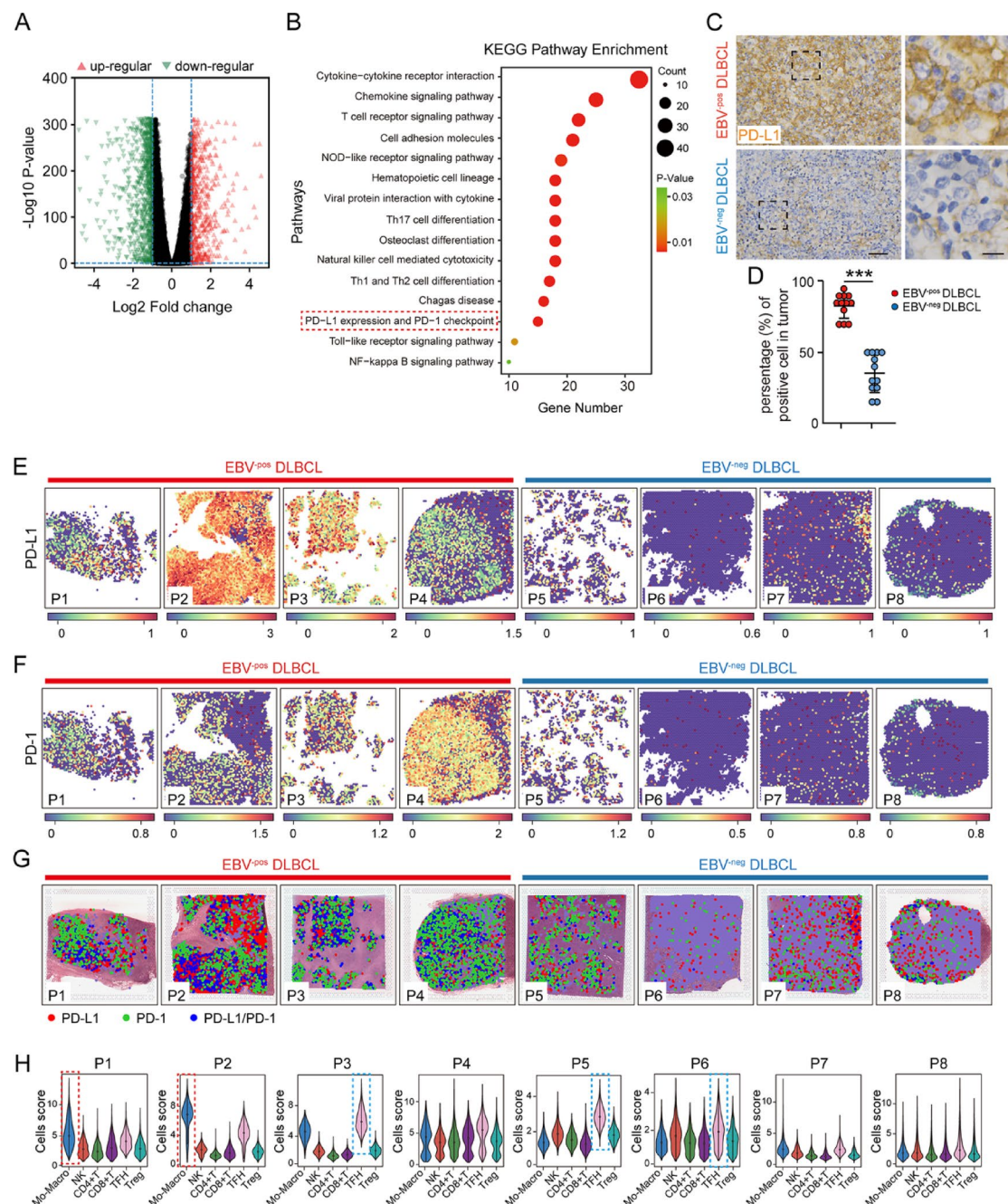


Fig. 3. Spatial expression patterns of the immune checkpoint molecules PD-1/PD-L1 in TMEs from EBV+DLBCL and EBV-DLBCL. **(A)** Differentially expressed gene (DEG) analysis of the region in tumors from EBV+ and EBV-DLBCL. **(B)** KEGG pathway enrichment analysis of DEGs. KEGG pathway maps were reproduced with permission from Kanehisa Laboratories. Copyright© Kanehisa Laboratories. **(C-D)** Representative PD-L1 (yellow) IHC staining of the transverse section images of lymph nodes from EBV+ and EBV-DLBCL **(C)**; scatter plot showing the comparisons of the percentage of PD-L1⁺ cells **(D)**. **(E-F)** Spatial feature plots of PD-L1 **(E)** and PD-1 **(F)** in each TME from EBV+ and EBV-DLBCL. **(G)** Spatial feature plots of immune checkpoint molecule PD-L1 (red) and PD-1 (blue) co-expression in each TME. **(H)** Violin plots of different cell type scores (Mo-Macro, NK, CD4⁺ T, CD8⁺ T, TFH and Treg cells) in each TME from EBV+ and EBV-DLBCL. The cluster with the highest average score is shown in the red dotted box. Mo-Macro, monocytes and macrophages; NK cells, natural killer cells; TFH cells, follicular helper T cells; Treg cells, regulatory T cells. Scale bars = 50 μ m in C left, 10 μ m in C right.

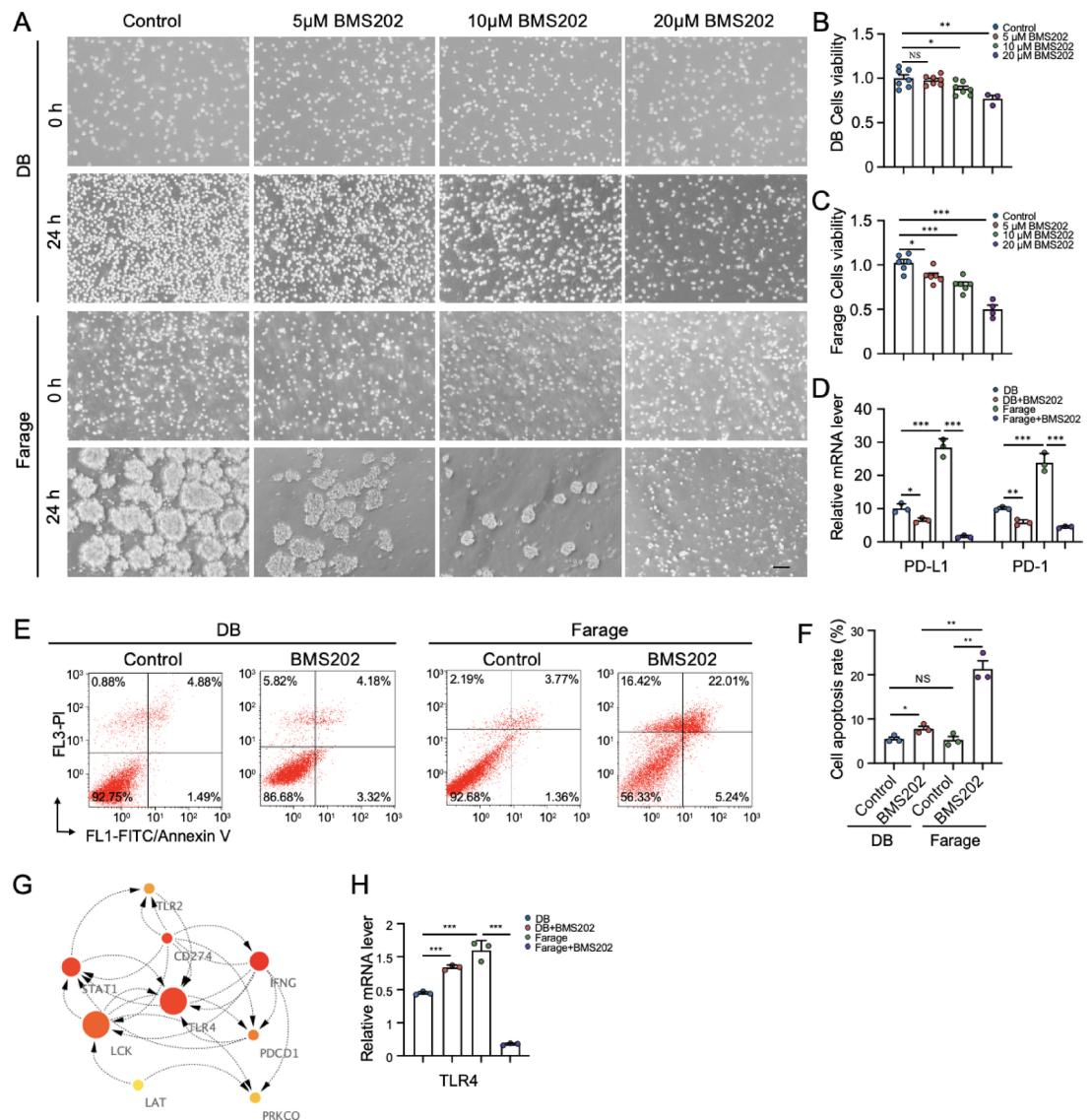


Fig. 4. To evaluate the impact of PD-1/PD-L1 signaling on DLBCL cells in the context of EBV infection. (A) The representative bright-field images were taken from control, 5 μM BMS202, 10 μM BMS202 and 20 μM BMS202 groups at incubation times of 0 and 24 h, respectively. (B–C). Bar chart showing the comparison of CCK8 values of DB or Farage cells incubated with/without BMS202. (D) The relative mRNA expression of PD-L1 and PD in DB or Farage cells from the aforementioned three groups ($n = 3$ per group). (E) The propidium iodide (PI) flow cytometric assay was implemented in 24-h incubated DB or Farage cells from control and 10 μM BMS202 group. (F) The bar chart showing the comparison of the values of late apoptosis (the upper right corner of the quadrant) + early apoptosis (the lower right corner of the quadrant) in the cultured DB or Farage cells among control and 10 μM BMS202 group. (G) Bioinformatics analysis depicting genes involved in this study, which were mapped using the STRING database to construct the protein-protein interaction network. (H) The relative mRNA expression of TLR4 in DB or Farage cells from the aforementioned three groups ($n = 3$ per group). Scale bars = 100 μm in A.

increased following BMS202 exposure ($p < 0.001$) (Fig. 4H). These divergent responses establish a functional link between PD-1/PD-L1 signaling and TLR4 regulation, particularly in Farage cells where pathway inhibition led to substantial TLR4 suppression.

Discussion

Accumulating research suggests that EBV+DLBCL typically presents with a diminished response to chemotherapy, less favorable recovery prospects, and lower survival rates^{3,23}, as corroborated by our clinical data (Table S1). This underscores the urgent need for novel treatment approaches. Current research into EBV+DLBCL has largely been centered on genetic alterations, with limited exploration into the TME. One investigation delineated the cellular makeup of the TME by synthesizing data from various single-cell studies and developing a machine

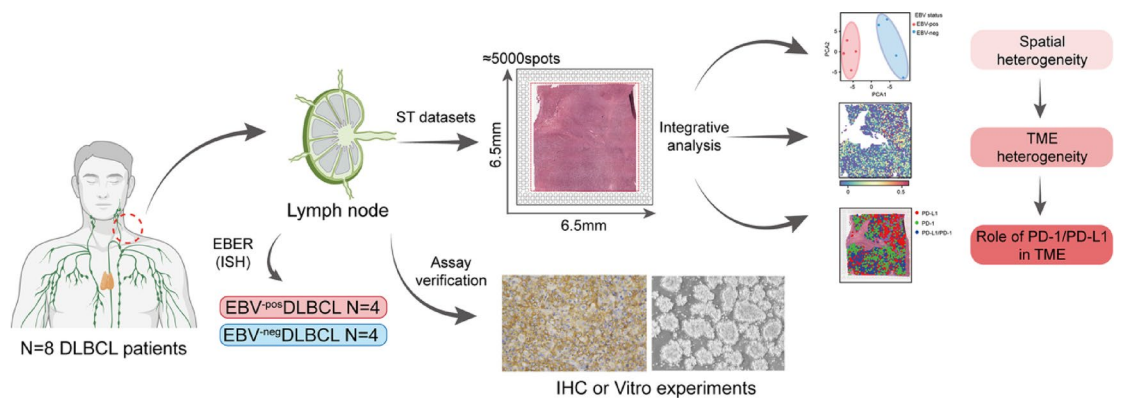


Fig. 5. Bioinformatics Analysis Workflow. This research utilized two types of datasets, namely, EBV+ and EBV-DLBCL. ST data were employed to investigate the role of PD-1/PD-L1 in immunosuppression within the TME of EBV+DLBCL. Subsequently, the bioinformatics findings were validated through IHC staining and Vitro experiments, confirming the pivotal functions of PD-1/PD-L1 in EBV+DLBCL.

learning construct known as EcoType⁹. In particular, Ye et al. charted single-cell landscapes of DLBCL, noting a B-cell subcluster called Bmemory-3, predominantly found in EBV+DLBCL cases, and associated with EBV infection²⁴. Nonetheless, this data does not incorporate spatial context. Our research firstly includes the analysis and juxtaposition of spatial gene expression in tissue samples from both EBV+ and EBV-DLBCL, uncovering marked disparities in cellular composition and spatial arrangement that could inform future pharmacological treatment strategies. We have encapsulated our research process in a detailed workflow (Fig. 5).

This study primarily investigates the spatial distribution characteristics of EBV+DLBCL through the application of ST technology (the first instance of its use in EBV+DLBCL thus far). Firstly, employing unsupervised dimensionality reduction clustering analysis across various tumor types and different patients (Fig. 1), the results indicate significant differences in cellular composition based on the EBV infection status. Research shows that though the exact mechanisms by which EBV initiates infection and fosters the development of associated tumors remain to be fully elucidated, it is acknowledged that EBV can craft a conducive environment by producing and releasing viral products that actively engage with immune cells in the TME. Moreover, the TME of an advancing tumor may, in certain cases such as EBV-associated Gastric Cancer, enhance the susceptibility to EBV infection. The infected cells are adept at creating an immunosuppressive milieu, employing various immune evasion tactics. Depending on the type of EBV-associated tumors, EBV can lead to a diverse composition of the TME. The extensively studied case is EBV+Hodgkin lymphoma (HL), where the TME plays a crucial role. Despite the lower immunogenicity of EBV+ tumor cells compared to lytically infected ones, they can still provoke EBV- specific immune responses. Studies have shown an increased presence of infiltrating CD4⁺ T cells, particularly Treg cells secreting IL10, as well as activated cytotoxic CD8⁺ T cells and NK cells in response to EBV²⁵. Additionally, EBV+ HL exhibits significantly higher numbers of tumor-associated macrophages compared to EBV- cases^{25,26}. While the cellular composition differences between EBV+ and EBV- as well as their spatial distribution, are currently unclear. Therefore, by leveraging ST in conjunction with published scRNA-seq data and applying deconvolution algorithms, our analysis reveals that, in comparison to the EBV-group, the stroma of EBV is enriched with a higher proportion of immune cells, predominantly macrophages (Fig. 2). Moreover, immune evasion in EBV-associated cancers may be triggered by the overexpression of PD-L1/PD-L2 and CTLA-4, leading to T cell exhaustion^{27–30}.

The present study demonstrates that pharmacological inhibition of the PD-1/PD-L1 signaling pathway using BMS202 exerts distinct effects on EBV+ and EBV-DLBCL cells (Figs. 3 and 4), providing mechanistic insights into the clinically observed differences in EBV-associated lymphomas. Recent clinical studies have established that EBV+DLBCL represents a distinct biological subtype characterized by an immunosuppressive tumor microenvironment (TME) and inferior outcomes following standard immunochemotherapy³¹. Our findings align with and extend these clinical observations, demonstrating that EBV+Farage cells exhibit enhanced sensitivity to PD-1/PD-L1 blockade compared to EBV-DB cells, mirroring the heightened PD-L1 expression patterns observed in clinical specimens³². The differential response to BMS202 treatment between EBV+ and EBV-cells may reflect fundamental differences in their dependence on PD-1/PD-L1 signaling. This is particularly relevant given recent evidence that EBV+DLBCL displays a unique TME profile with elevated immune checkpoint expression³¹, including the PD-1/PD-L1 axis which contributes to CD8+ T cell exhaustion³³. Our identification of TLR4 as a downstream mediator of PD-1/PD-L1 signaling in EBV+ cells provides a potential molecular link between immune checkpoint regulation and the characteristic immunosuppressive features of EBV-associated lymphomas, including elevated IL-10 levels^{33–35} and impaired cytotoxic T cell function³⁶.

The robust apoptotic response observed in Farage cells following PD-1/PD-L1 inhibition has important therapeutic implications, particularly in the context of emerging treatment strategies for refractory DLBCL. While R-CHOP remains standard first-line therapy with significant cure rates, approximately one-third of patients experience relapse with poor outcomes³⁷. Our findings support the rationale for combining PD-1/PD-L1 inhibitors with novel therapies like CAR-T cells especially in EBV+ cases where the immunosuppressive TME

may limit treatment efficacy. The differential TLR4 regulation we observed between EBV+ and EBV-cells further suggests that targeted approaches may need to be tailored based on EBV status.

These results must be interpreted in the context of EBV's complex biology and its varied latency patterns across different malignancies. While our study focused on PD-1/PD-L1 inhibition, the presence of multiple immune checkpoints (e.g., LAG3, TIM3) and alternative immunosuppressive mechanisms (e.g., M2 macrophage polarization)³¹ suggests that combination strategies targeting multiple pathways may be required to effectively overcome the immunosuppressive TME in EBV-associated lymphomas.

Despite the promise shown in this research, our study has several technical limitations inherent to spatial transcriptomics. First, the resolution of 10x Visium (~55 µm/spot, typically capturing 1–10 cells per spot) may obscure single-cell-level heterogeneity, particularly in mixed-cell regions. While this platform provides valuable spatial insights, its precision falls short of single-cell sequencing. To address this, we integrated our ST data with published DLBCL scRNA-seq data⁹ using Cell2location²¹, which significantly improved cell-type annotation accuracy compared to morphological region-based methods. This approach revealed layered cellular subpopulations and their potential interactions, demonstrating the algorithm's suitability for ST analysis. Second, although we observed high reproducibility across replicates (Fig. S4), batch effects from sample processing could influence cross-sample comparisons. To mitigate this, we performed data integration and batch effect correction using Harmony on PCA embeddings, which effectively aligned samples across different batches while preserving biological variation (Fig. S2). Finally, low-abundance transcripts may be underrepresented due to dropout effects. Future studies with single-cell resolution platforms could address these limitations. In addition, we acknowledge that our sample size ($n=4$ per group), while consistent with field standards^{38–40}, limits generalizability. This constraint stems from the rarity of surgically resected samples with matched clinicopathological data, a common challenge in ST studies. Nevertheless, the high data density (~5,000 spatially resolved spots per sample) and in-vitro validation (Fig. 4) validation strengthen confidence in our results.

In summary, we have conducted the inaugural measurement and comparison of spatial gene expression within tissue slices of EBV+DLBCL and EBV-DLBCL. Simultaneously, we have illustrated the landscape of the TME and its diverse components by integrating single-cell and spatial transcriptome technologies and assess the expression of PD-1 and PL-L1, revealing that the poor prognosis of EBV+DLBCL may be related to the TME heterogeneity and PD-1/PD-L1 pathways. It is obvious that this discovery offers the pharmacological treatment strategies basis for improving therapy for personalized analysis. Our study provides experimental evidence supporting the clinical development of PD-1/PD-L1 inhibitors for EBV+DLBCL and identifies TLR4 as a potential mediator of treatment response. These findings contribute to our understanding of EBV-driven lymphomagenesis and suggest that therapeutic strategies targeting the PD-1/PD-L1-TLR4 axis may help overcome the immunosuppressive TME characteristic of these aggressive lymphomas. Future studies should explore optimal combination approaches and validate TLR4 as a predictive biomarker in clinical cohorts.

Data availability

All data generated in this study have been uploaded to <https://www.biosino.org/node/browse?keyword=OEP0004742>.

Received: 13 December 2024; Accepted: 28 April 2025

Published online: 07 May 2025

References

- Ross, A. M. et al. Epstein–Barr virus and the pathogenesis of diffuse large B-Cell lymphoma. *Life* **13**, 521 (2023).
- Yiwei, G. & Aichun, L. Treatment of EB virus positive diffuse large B cell lymphoma. *J. Int. Oncol.* **48**, 385 (2021).
- Bourbon, E. et al. Clinicopathological features and survival in EBV-positive diffuse large B-cell lymphoma not otherwise specified. *Blood Adv.* **5**, 3227–3239 (2021).
- Liu, F. et al. Genetic heterogeneity and mutational signature in Chinese Epstein–Barr virus-positive diffuse large B-cell lymphoma. *PLoS One.* **13**, e0201546 (2018).
- Jamal-Hanjani, M., Quezada, S. A., Larkin, J. & Swanton, C. Translational implications of tumor heterogeneity. *Clin. Cancer Res.* **21**, 1258–1266 (2015).
- McGranahan, N. et al. Clonal status of actionable driver events and the timing of mutational processes in cancer evolution. *Sci. Transl. Med.* **7**, 283ra254–283ra254 (2015).
- McGranahan, N. & Swanton, C. Clonal heterogeneity and tumor evolution: past, present, and the future. *Cell* **168**, 613–628 (2017).
- Lee, H., Yoon, S. E., Kim, S. J., Kim, W. S. & Cho, J. A unique expression pattern of LAG3 distinct from that of other immune checkpoints in diffuse large B-cell lymphoma. *Cancer Med.* <https://doi.org/10.1002/cam4.6268> (2023).
- Steen, C. B. et al. The landscape of tumor cell states and ecosystems in diffuse large B cell lymphoma. *Cancer Cell* **39**, 1422–1437 e1410, (2021). <https://doi.org/10.1016/j.ccell.2021.08.011>
- Stahl, P. L. et al. Visualization and analysis of gene expression in tissue sections by Spatial transcriptomics. *Science* **353**, 78–82 (2016).
- Rodrigues, S. G. et al. Slide-seq: A scalable technology for measuring genome-wide expression at high Spatial resolution. *Science* **363**, 1463–1467 (2019).
- Vickovic, S. et al. High-definition Spatial transcriptomics for in situ tissue profiling. *Nat. Methods.* **16**, 987–990 (2019).
- Singel, K. L. et al. Mature neutrophils suppress T cell immunity in ovarian cancer microenvironment. *JCI Insight* **4** (2019).
- Swerdlow, S. H. et al. The 2016 revision of the world health organization classification of lymphoid neoplasms. *Blood J. Am. Soc. Hematol.* **127**, 2375–2390 (2016).
- Nocturne, G. et al. Impact of anti-TNF therapy on NK cells function and on immunosurveillance against B-cell lymphomas. *J. Autoimmun.* **80**, 56–64 (2017).
- He, M. et al. Nrf2 is involved in hyperglycemia-induced abnormal lung development through both antioxidation-dependent and antioxidation-independent activation. *Am. J. Respir. Cell Mol. Biol.* **69**, 197–209 (2023).
- Maynard, K. R. et al. Transcriptome-scale Spatial gene expression in the human dorsolateral prefrontal cortex. *Nat. Neurosci.* **24**, 425–436. <https://doi.org/10.1038/s41593-020-00787-0> (2021).
- Korsunsky, I. et al. Fast, sensitive and accurate integration of single-cell data with harmony. *Nat. Methods.* **16**, 1289–1296 (2019).

19. Kanehisa, M. & Goto, S. KEGG: Kyoto encyclopedia of genes and genomes. *Nucleic Acids Res.* **28**, 27–30 (2000).
20. Kanehisa, M., Furumichi, M., Sato, Y. & Kawashima, M. Ishiguro-Watanabe, M. KEGG for taxonomy-based analysis of pathways and genomes. *Nucleic Acids Res.* **51**, D587–D592 (2023).
21. Kleshchevnikov, V. et al. Cell2location maps fine-grained cell types in Spatial transcriptomics. *Nat. Biotechnol.* **40**, 661–671 (2022).
22. Pham, D. et al. stLearn: integrating spatial location, tissue morphology and gene expression to find cell types, cell-cell interactions and spatial trajectories within undissociated tissues. *BioRxiv*, 2005. 2031.125658 (2020). (2020).
23. GUO, Y. & LIU, A. Treatment of EB virus positive diffuse large B cell lymphoma. *J. Int. Oncol.*, 385–388 (2021).
24. Ye, X. et al. A single-cell atlas of diffuse large B cell lymphoma. *Cell. Rep.* **39**, 110713. <https://doi.org/10.1016/j.celrep.2022.110713> (2022).
25. Kamper, P. et al. Tumor-infiltrating macrophages correlate with adverse prognosis and Epstein-Barr virus status in classical Hodgkin's lymphoma. *Haematologica* **96**, 269 (2011).
26. Barros, M. H. M., Hassan, R. & Niedobitek, G. Tumor-associated macrophages in pediatric classical hodgkin lymphoma: association with Epstein-Barr virus, lymphocyte subsets, and prognostic impact. *Clin. Cancer Res.* **18**, 3762–3771 (2012).
27. Green, M. R. et al. Constitutive AP-1 activity and EBV infection induce PD-L1 in hodgkin lymphomas and posttransplant lymphoproliferative disorders: implications for targeted therapy. *Clin. Cancer Res.* **18**, 1611–1618 (2012).
28. Derks, S. et al. Abundant PD-L1 expression in Epstein-Barr Virus-infected gastric cancers. *Oncotarget* **7**, 32925 (2016).
29. Saito, R. et al. Overexpression and gene amplification of PD-L1 in cancer cells and PD-L1 + immune cells in Epstein-Barr virus-associated gastric cancer: the prognostic implications. *Mod. Pathol.* **30**, 427–439 (2017).
30. Huang, P. Y. et al. Tumor CTLA-4 overexpression predicts poor survival in patients with nasopharyngeal carcinoma. *Oncotarget* **7**, 13060 (2016).
31. Keane, C. et al. The tumour microenvironment is immuno-tolerogenic and a principal determinant of patient outcome in EBV-positive diffuse large B-cell lymphoma. *Eur. J. Haematol.* **103**, 200–207 (2019).
32. Kanegane, H., Nomura, K., Miyawaki, T. & Tosato, G. Biological aspects of Epstein-Barr virus (EBV)-infected lymphocytes in chronic active EBV infection and associated malignancies. *Crit. Rev. Oncol. Hematol.* **44**, 239–249 (2002).
33. Quan, L. et al. PD-1 Blockade can restore functions of T-cells in Epstein-Barr virus-positive diffuse large B-cell lymphoma in vitro. *PLoS One.* **10**, e0136476 (2015).
34. Tan, G. W., Visser, L., Tan, L. P., van den Berg, A. & Diepstra, A. The microenvironment in Epstein-Barr virus-associated malignancies. *Pathogens* **7**, 40 (2018).
35. Cohen, M. et al. Cytotoxic response against epstein barr virus coexists with diffuse large B-cell lymphoma tolerogenic microenvironment: clinical features and survival impact. *Sci. Rep.* **7**, 10813 (2017).
36. Cárdenas, D. et al. Epstein-Barr virus-specific CD8 + T lymphocytes from diffuse large B cell lymphoma patients are functionally impaired. *Clin. Experimental Immunol.* **182**, 173–183 (2015).
37. Mondello, P. & Mian, M. Frontline treatment of diffuse large B-cell lymphoma: beyond R-CHOP. *Hematol. Oncol.* **37**, 333–344 (2019).
38. Scott, E. Y. et al. Integrating single-cell and spatially resolved transcriptomic strategies to survey the astrocyte response to stroke in male mice. *Nat. Commun.* **15**, 1584 (2024).
39. Oliveira, M. F. et al. Characterization of immune cell populations in the tumor microenvironment of colorectal cancer using high definition spatial profiling. *BioRxiv*, 2006. 2004.597233 (2024). (2024).
40. Huuki-Myers, L. A. et al. A data-driven single-cell and Spatial transcriptomic map of the human prefrontal cortex. *Science* **384**, eadh1938 (2024).

Acknowledgements

This study was supported by China Postdoctoral Science Foundation grant 2023M730596 and 14th Five-year high level specialty construction project in Foshan FSGSP145033.

Author contributions

All authors contributed to the study conception and design. Mei-yao He, Meng Liu and Jiayin Yuan, designed, performed experiments, and draft the manuscript. Jin Lv and Wei Li, interpreted the results. Qianwen Yan, Yujiao Tang, Luyi Wang and Li Guo, conceived the study and designed experiments. Fang Liu wrote and revised the manuscript. All authors have read the manuscript and approved the study.

Declarations

Competing interests

The authors declare no competing interests.

Additional information

Supplementary Information The online version contains supplementary material available at <https://doi.org/10.1038/s41598-025-00410-x>.

Correspondence and requests for materials should be addressed to F.L.

Reprints and permissions information is available at www.nature.com/reprints.

Publisher's note Springer Nature remains neutral with regard to jurisdictional claims in published maps and institutional affiliations.

Open Access This article is licensed under a Creative Commons Attribution-NonCommercial-NoDerivatives 4.0 International License, which permits any non-commercial use, sharing, distribution and reproduction in any medium or format, as long as you give appropriate credit to the original author(s) and the source, provide a link to the Creative Commons licence, and indicate if you modified the licensed material. You do not have permission under this licence to share adapted material derived from this article or parts of it. The images or other third party material in this article are included in the article's Creative Commons licence, unless indicated otherwise in a credit line to the material. If material is not included in the article's Creative Commons licence and your intended use is not permitted by statutory regulation or exceeds the permitted use, you will need to obtain permission directly from the copyright holder. To view a copy of this licence, visit <http://creativecommons.org/licenses/by-nc-nd/4.0/>.

© The Author(s) 2025